



FULL ARTICLE

Simultaneous cell traction and growth measurements using light

Shamira Sridharan Weaver^{1,2}  | Yanfen Li^{2,3} | Louis Foucard⁴ | Hassaan Majeed^{1,2} | Basanta Bhaduri¹ | Alex J. Levine^{4,5,6} | Kristopher A. Kilian^{2,3} | Gabriel Popescu^{1,2,7*} 

¹Quantitative Light Imaging Laboratory, Beckman Institute for Advanced Science and Technology, University of Illinois at Urbana-Champaign, Urbana, Illinois

²Department of Bioengineering, University of Illinois at Urbana-Champaign, Urbana, Illinois

³Department of Material Science and Engineering, University of Illinois at Urbana-Champaign, Urbana, Illinois

⁴Department of Chemistry and Biochemistry, University of California, Los Angeles, California

⁵Department of Physics & Astronomy, University of California, Los Angeles, California

⁶Department of Biomathematics, University of California, Los Angeles, California

⁷Department of Electrical and Computer Engineering, University of Illinois at Urbana-Champaign, Urbana, Illinois

*Correspondence

Gabriel Popescu, Quantitative Light Imaging Laboratory, Beckman Institute for Advanced Science and Technology, University of Illinois at Urbana-Champaign, Urbana, IL 61801.
Email: gpopescu@illinois.edu

Present address

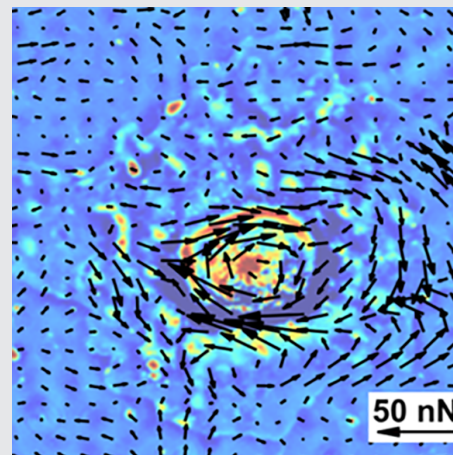
Shamira Sridharan Weaver, Department of Urologic Surgery, University of California, Davis, Sacramento, CA 95817.

Kristopher A. Kilian, School of Chemistry, School of Materials Science and Engineering, Australian Centre for NanoMedicine, The University of New South Wales, Sydney, NSW 2052, Australia.

Funding information

National Institutes of Health, Grant/Award Number: HL12175; National Science Foundation (US), Grant/Award Number: IIP-1353368; National Science Foundation, Grant/Award Numbers: CBET-0939511 STC, DBI 14-50962 EAGER, DMR-1309188, 1454616 CAR, DGE - 1144245

Characterizing the effects of force fields generated by cells on proliferation, migration and differentiation processes is challenging due to limited availability of nondestructive imaging modalities. Here, we integrate a new real-time traction stress imaging modality, Hilbert phase dynamometry (HPD), with spatial light interference microscopy (SLIM) for simultaneous monitoring of cell growth during differentiation processes. HPD uses holographic principles to extract displacement fields from chemically patterned fluorescent



grid on deformable substrates. This is converted into forces by solving an elasticity inverse problem. Since HPD uses the epi-fluorescence channel of an inverted microscope, cellular behavior can be concurrently studied in transmission with SLIM. We studied the differentiation of mesenchymal stem cells (MSCs) and found that cells undergoing osteogenesis and adipogenesis exerted larger and more dynamic stresses than their precursors, with MSCs developing the smallest forces and growth rates. Thus, we develop a powerful means to study mechanotransduction during dynamic processes where the matrix provides context to guide cells toward a physiological or pathological outcome.

KEYWORDS

mass, quantitative phase imaging, stem cells, traction force

1 | INTRODUCTION

Cells and their microenvironment interact through a complex combination of pushing and pulling forces that in turn affect

processes such as cell adhesion, migration, proliferation and differentiation [1]. The cytoskeletal network, which is made up by filamentous actin, intermediate filaments and microtubules, mediates the transmission of forces within the cell [2]. The cytoskeletal elements bind to focal adhesion (FA) proteins at the cell membrane that in turn mediate interactions with the

Shamira Sridharan Weaver, Yanfen Li and Louis Foucard contributed equally in this study.

extracellular matrix (ECM) through cell surface integrins. The mechanical forces generated at these interfaces influence biochemical signaling, in a process termed *mechanotransduction*, which has important implications on cell fate, and downstream tissue form and function [3]. An FA, thus, serves as both the point at which the cell may exert forces on its surroundings and as the cell's window into mechanical changes occurring in the surrounding tissue, leading to adaptive changes within the cell. Understanding mechanotransduction is especially critical in cancer cell biology, where processes such as cell lamellipodia extension, migration and angiogenesis, are mediated through interactions with the surrounding ECM and can dramatically influence the aggressiveness and metastatic potential of the cancer [4–7]. In addition to pathological processes, during normal development, mechanochemical signals regulate stem cell lineage determination, where the ECM provides context to guide the integration of multiple cues from the microenvironment. Stem cells show a degree of lineage plasticity and can shift their state through interrogation of ECM mechanics and composition. The mechanical interactions between stem cells and their environment influences proliferation, migration and differentiation, toward the regulation of wound healing, tissue morphogenesis and homeostasis [8–11].

In recent years, significant progress has been reported in the development of quantitative techniques to measure cell-generated forces (see Ref. [12] for a recent review). These methods can be broadly classified into two categories: *active*, that is, based on measuring the response of the cell to application of external forces, and *passive*, built on measuring the substrate deformation due to intrinsic, cell-generated forces. Common methods within the first category are atomic force microscopy, optical tweezers and magnetic tweezers [13–16]. However, these methods suffer from the limitations in spatial sampling and restrictive thresholds for the measurable forces. *Traction force microscopy* techniques that have gained the most widespread adoption employ micropatterned pillars, textured substrates and coated fluorescent beads. Traction forces from micropillar arrays are calculated from the bending of soft pillars of known mechanical properties [17, 18]. However, by restricting the cell adhesion sites to the locations of the micropatterned pillars, this technique is not an ideal representation of two-dimensional (2D) cell culture. A digital holography-based technique that also uses pillars to measure traction forces has been developed; however, a more valuable application of this technique lies in studying the assembly and internal cell behavior around the adhesion sites [19]. Substrate deformation measured from textured polydimethylsiloxane (PDMS) substrates are an alternative method [20]. This technique requires fluorescent tagging of the FA sites within the cell. A similar method looks at the displacement of topographically patterned dots; however, the method has multiple shortcomings from computational assumptions including limited spatial resolution, and the requirement that one observe single cells, or, at least, cells with high degree of spatial separation [21]. Another established

approach involves the incorporation of fluorescently tagged beads within an elastic substrate to study the traction of multiple cells [22, 23]. However, this method requires the removal of cells from the substrate surface in order to obtain the initial configuration of the incorporated beads, which is a tedious and error-prone process. Recently, other fluorescence-based approaches includes *confocal* traction force microscopy which relies on nanodrip-printed monocrystalline array of fluorescent quantum dots [24] or super-resolved traction force microscopy which uses stimulated emission depletion microscopy to measure displacement of fluorescent beads [25]. These approaches alleviate some of the previous limitations, but at the same time rely on specialized, high-precision substrate preparation, require expensive setups, and retain the need for fluorescent particles. Holographic traction force microscopy measures traction force without the need of fluorescent particles yet still requires non-fluorescent beads embedded within polyacrylamide (PA) hydrogels thus retaining the need for tracking individual particles [26].

Here, we present a multimodal microscopy-based approach that monitors cell growth using spatial light interference microscopy (SLIM) in transmission simultaneously with cell-generated traction force monitoring in epi-fluorescence mode through a novel technique we developed called Hilbert phase dynamometry (HPD). SLIM [27–30] performs mass measurements through quantitative phase imaging (QPI) of live mesenchymal stem cells (MSCs) in unperturbed culture under three different conditions: no treatment, adipogenic differentiation and osteogenic differentiation. QPI is an emerging field of label-free imaging that has found important applications in biomedicine [31]. Phase sensitive methods have been applied before to studying dynamics in cellular systems [32–34]. Among other applications, studying cell growth has perhaps the broadest potential ramifications as it addresses this “long-standing question in biology” [35]. The label-free nature of SLIM measurements in the transmission channel of a conventional microscope allows for using the epi-fluorescence channel for force measurements using HPD. HPD measures forces exerted by cells in *real time*, over extended periods of time. The cells are grown on flat, deformable substrates with a customized 2D fluorescent adhesion protein grid patterned at sub-cellular resolution. The in-plane displacement field is continuously measured with high spatial and temporal resolution. The adherent cell-induced strain field is contained in the 2D phase map of the complex analytical signal associated with the periodic grid. The key principle of HPD is rooted in calculation of displacement fields using the principles of phase reconstruction used in *off-axis holography*, as developed by Leith and Upatnieks [36] (for a review on phase reconstruction and imaging, see also Ref. [31]). From the displacement field, we solve the *inverse* elasticity problem and extract a traction force vector field. As the fluorescent grid is patterned for uniform sampling of the substrate, HPD eliminates the need for tracking individual particles. It can also monitor cell behavior

continuously, without removing the cells from culture. Thus, through synchronized channel switching on the microscope, we are able to simultaneously measure cell growth and traction forces using SLIM and HPD, respectively, during stem cell differentiation. We used MSCs as a model because it is an adherent adult stem cell line that shows high responsivity to ECM properties [22, 37–39]. Our results show that cells undergoing differentiation, osteogenesis and adipogenesis, exerted larger and more dynamic stresses than their precursor. In addition, MSCs exert the smallest forces and have the lowest growth rates compared to their differentiated progeny. Thus, by using integrated HPD-SLIM system, we uncover the relationship between MSC generated traction, growth and differentiation.

2 | RESULTS

2.1 | Technique development: HPD

HPD relies on the extraction of displacement maps of adhesion proteins on a deformable substrate using holographic principles and solving the inverse elasticity problem. The preparation of substrates for retrieval of cell-induced deformation fields and thus, HPD-based force calculations, is illustrated in Figure 1. First, the 10 kPa stiffness PA gel is chemically activated and stamped with fluorescein isothiocyanate (FITC)-conjugated adhesion protein, to create a 9 μm period grid in both x and y directions (see Figure 1A,B, details on the gel preparation in Section 6 and Section S3 in Appendix S1, Supporting Information). The substrate is then uniformly exposed to nonfluorescent fibronectin to ensure homogeneous cell adhesion to the substrate (Figure 1C). In this way, FITC-conjugated and non-FITC-conjugated adhesion proteins are placed in alternating intervals, such that the cells do not sense the grid and, upon traction, generate bending of the substrate in both directions. The cells were seeded and allowed to settle on the substrate for an hour before imaging in epi-fluorescence mode for extraction of displacement maps (Figure 1D).

2.2 | Calculation of displacement maps

The deformations in the substrate are measured from the phase of the 2D periodic signal associated with the fluorescence measurements of the grid (Figure 2A). The image of the 9 μm periodicity fluorescent protein grid used in this study is shown in Figure 2B and the absolute value of its Fourier transform is shown in Figure 2C. Because the grid is not perfectly sinusoidal in shape, the Fourier transform of its image generates multiple orders along each direction laterally (x , y directions). However, if we only retain the first orders in both x and y directions, the analysis is equivalent to that of a perfect sinusoidal grid. The signal of interest along each direction has the form

$$R_{x,y} = A \cos [\beta x + \phi_{x,y}(x,y)], \quad (1)$$

where $R_{x,y}$ are the sinusoidal fluorescence intensities (real value of the signals) along x and y , $\phi_{x,y}(x,y)$ the respective phases that incorporate the displacement information, and β is the spatial frequency of the grid, $\beta = 2\pi/9$ rad/ μm (see Section S1 in Appendix S1 for more details). We apply a spatial frequency filter that selects the first order in the x and y directions, as shown in Figure 2D,E, respectively. Inverse Fourier transform of the signals in Figure 2D,E results in complex signals, namely, the *complex analytic signals* associated with $R_{x,y}$. The concept of the complex analytic signal associated with a real optical field was exploited early on by Gabor [40] and served as foundation for his development of holography [41]. These two complex signals, one for each direction, are derived from the fluorescent protein grid image via the following expressions:

$$z_x(x,y) = R_x(x,y) + \frac{i}{\pi} P \int_{-\infty}^{\infty} \frac{R_x(x',y)}{x-x'} dx', \quad (2a)$$

$$z_y(x,y) = R_y(x,y) + \frac{i}{\pi} P \int_{-\infty}^{\infty} \frac{R_y(x,y')}{y-y'} dy', \quad (2b)$$

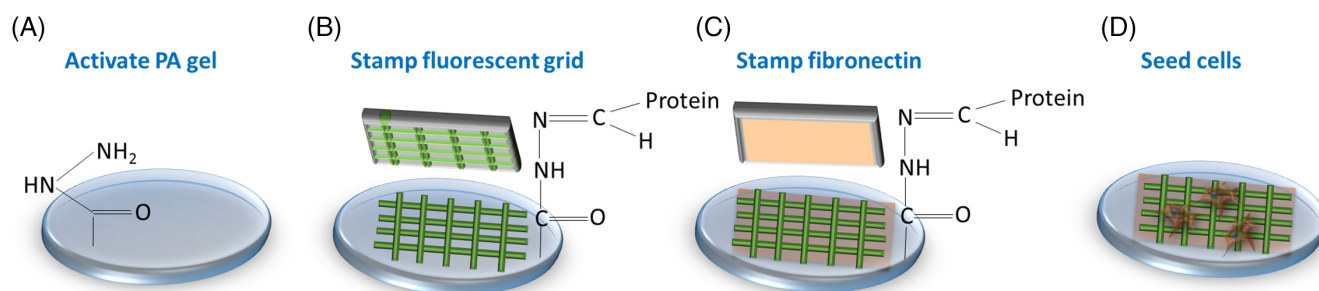


FIGURE 1 Engineering of PA hydrogels for traction force measurements using HPD. (A) PA hydrogels are activated with hydrazine hydrate to form hydrazide groups for conjugation of extracellular matrix proteins. (B) A fluorescent grid of 9 μm spacing containing a mixture of 25 $\mu\text{g}/\text{mL}$ fibronectin and 25 $\mu\text{g}/\text{mL}$ FITC-conjugated fibrinogen is stamped onto the activated hydrogel using a PDMS stamp. (C) Blank PDMS stamp with 25 $\mu\text{g}/\text{mL}$ fibronectin is used to fill the hydrogel with nonfluorescent adhesion proteins. (D) Cells are seeded onto the gel with uniform distribution of adhesion of proteins, and allowed to attach before measurements

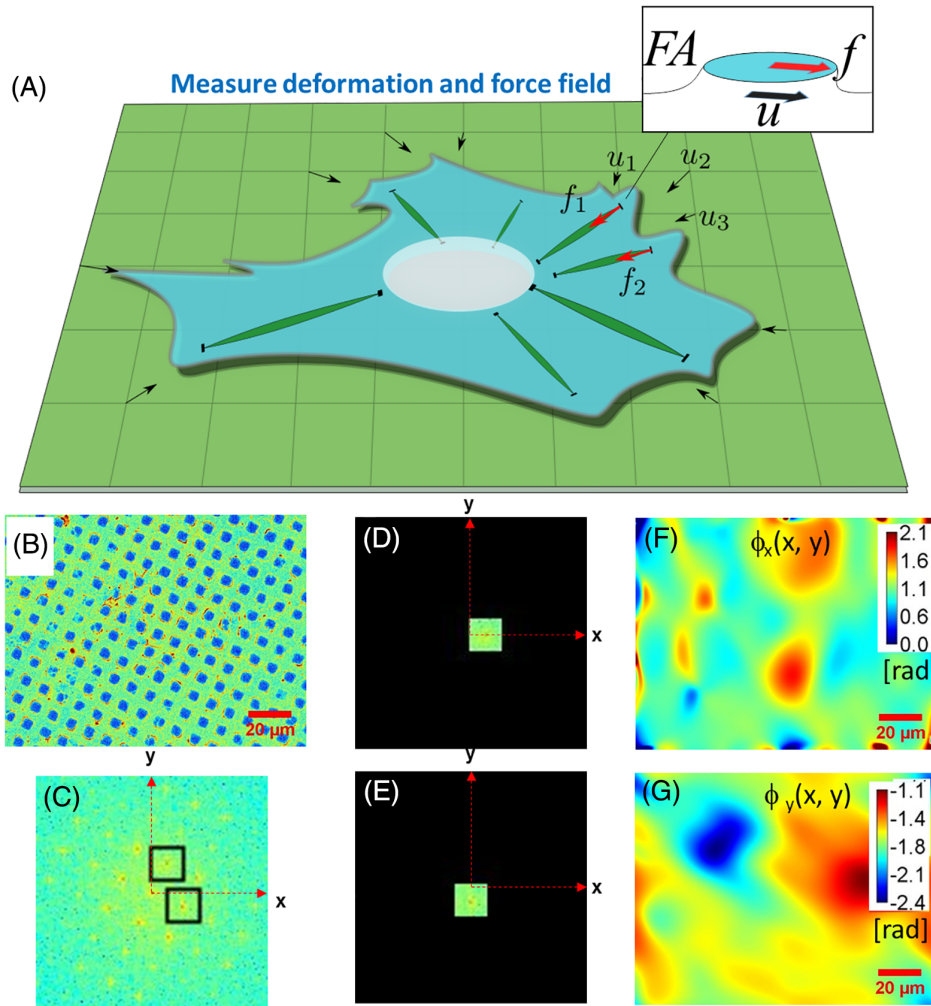


FIGURE 2 Schematic illustration of the process to reconstruct the lateral displacement map (X and Y displacements). (A) The traction force f exerted by the cell on the substrate can be retrieved by measuring the resulting substrate deformation u . (B) The raw fluorescence image of the engineered hydrogel with $9 \mu\text{m}$ spacing fluorescent adhesion protein grid. (C) Fourier transform of the fluorescence image of the hydrogel. (D-E) Zooming into the central region of the Fourier transform shows well separated orders in X and Y due to the periodicity of the grid. The spectrum is band-pass filtered over the regions shown. (F-G) Inverse Fourier transform of selected orders in D, E generates the phase shift maps of displacements along the x and y axes

where P stands for principal value integral. The sequence of performing a Fourier transform of the real signal, spatial filtering, followed by inverse Fourier transform back to the spatial domain, is a Hilbert transform [42], which is captured in the HPD acronym. The argument of each signal provides the deformation of the grid at each point in the field of view along each direction, $\phi_{x, y} = \arg(z_{x, y})$. The phase maps associated with the grid in Figure 2B are shown in Figure 2F,G, respectively. This phase information, in radians, is converted into spatial displacement, u , in microns, by noting that 2π radians corresponds to a displacement of a grid period, namely

$$u_{x,y} = \frac{\Lambda}{2\pi} \phi_{x,y}, \quad (3)$$

where Λ is the period, $\Lambda = 9 \mu\text{m}$. The minimum change in displacement was estimated as the phase noise in the time lapse images, which yielded a value of 0.23 rad in phase. Thus, the sensitivity for displacement measurements using this technique is $0.33 \mu\text{m}$.

2.3 | Calculation of force fields

The force field is extracted from the deformation map by solving a linear *Cerruti-type inverse problem* (Figure 2A and see Section 6 and Section S2 in Appendix S1 for details) [43]. Due to the linearity of the problem, the 2D displacement field u at position x and a disk distributed force of density f applied at an arbitrary position x' are related via a simple matrix-vector multiplication:

$$u(x) = G^{\text{disk}}(x-x') \cdot f. \quad (4)$$

In Eq. (4), the 2×2 matrix G^{disk} is a response (or transfer) function that describes the displacement response of the substrate, and is obtained by solving a Cerruti-type problem [43] (see Figure 3A-C and Section S2 in Appendix S1 for details on the derivation). We used disk distributed forces to represent the traction forces applied by the cell at FA sites. If one were given the locations of all FAs and the tractions that they produce, the surface displacements are then computed from the sum of the displacements

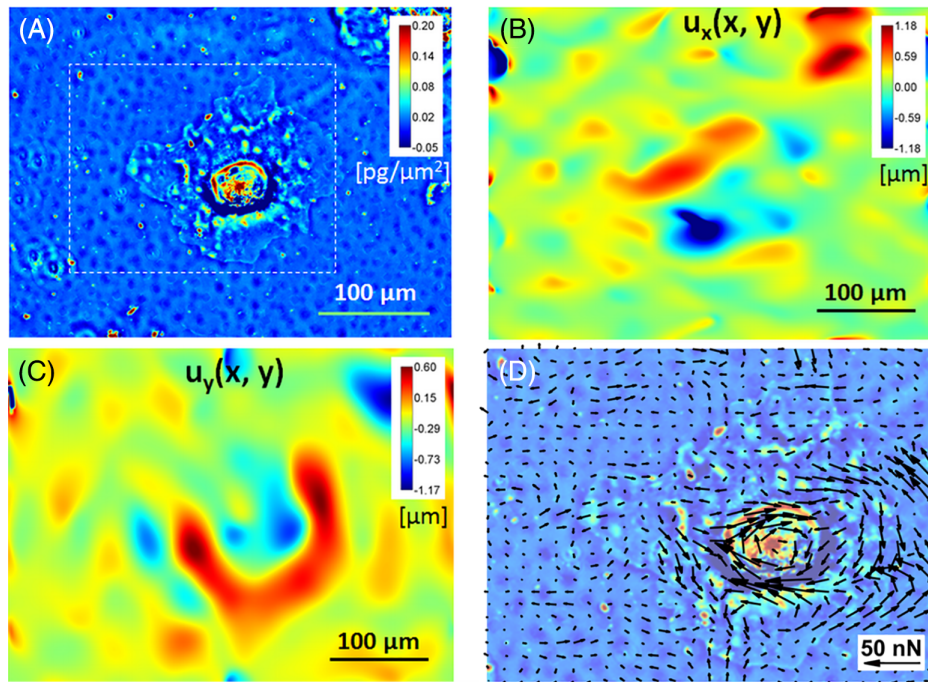


FIGURE 3 Calculation of force field from lateral displacement maps. (A) Quantitative phase image of a cell (adipocyte) on PA hydrogel coated with 2D fluorescent fibronectin grid at 9 μm periodicity at the beginning of the experiment. (B) X displacement map calculated from the phase map of the fluorescent grid deformations. (C) Y displacement map calculated from the phase map of the fluorescent grid deformations. (D) Cell traction force calculated from the X, Y displacement maps by solving an inverse linear Cerruti-type elasticity problem is overlaid on the image of the cell. $N = 3$, 43 images collected from each distinct sample with SLIM system. This experiment was replicated three times

associated with each FA separately, as shown in Eq. (4). Given a measured displacement map of size $N \times N$, and a grid of hypothetical FAs position of size $M \times M$ (with $M \leq N$), the problem of finding the forces exerted by the cell on these FAs can be written as the following linear system:

$$\begin{matrix} U \\ 2N^2 \times 1 \end{matrix} = \begin{matrix} G_{\text{tot}}^{\text{disk}} \\ 2N^2 \times 2M^2 \end{matrix} \cdot \begin{matrix} F \\ 2M^2 \times 1 \end{matrix}. \quad (5)$$

In Eq. (5), $G_{\text{tot}}^{\text{disk}}$ represents the summed response functions between multiple displacements and forces position. Finally, the force field F is computed by inverting the system above using a least square approximation, which concludes the HPD procedure. Figure 3D shows the force field calculated by HPD overlaid on the image of the cell. Videos S1-S6 illustrate the work flow for real-time calculations of force fields from the displacement maps for several cells.

3 | MICROSCOPY: SYNCHRONIZED CELL MASS AND FORCE MEASUREMENTS

The experimental setup for simultaneous measurement of cell mass and cell-induced traction forces, by software-based synchronization of SLIM and HPD are shown in Figure 4A. The measurements were performed with an inverted microscope, outfitted with both a SLIM module (Cell Vista SLIM Pro; Phi Optics, Inc., Champaign, Illinois),

and an epi-fluorescence optical train (see Figure 4A and Section 6 for further information on the optics) [44]. The epi-fluorescence channel provides images of the FITC-conjugated adhesion protein grid, while SLIM renders quantitative phase images in trans-illumination, which can be further analyzed in terms of cell dry mass density [30]. SLIM exploits the intrinsic refractive index contrast in live cells and is therefore, label-free enabling cell imaging over many hours without negative effects on cell viability. The SLIM and fluorescence channels are overlaid at the pixel level because of the common optical train used for measurements and hence, there is no need for computationally expensive registration algorithms.

The microscope can switch between the fluorescence and SLIM channels in 0.7 seconds, which makes it particularly appealing for studying traction and cell growth simultaneously. This multimodal setup can be programmed to scan large fields of view in the lateral direction (x - y), acquire depth scans (z -stack), as well as acquire images over variable time lines (seconds to days) at prespecified intervals (fraction of seconds to hours).

4 | APPLICATION: INTERACTION BETWEEN TRACTION FORCES AND GROWTH DURING MSC DIFFERENTIATION

We cultured bone marrow derived MSCs, and then subjected them to media containing soluble supplements supporting adipogenesis or osteogenesis for 1 week (see Section 6 for

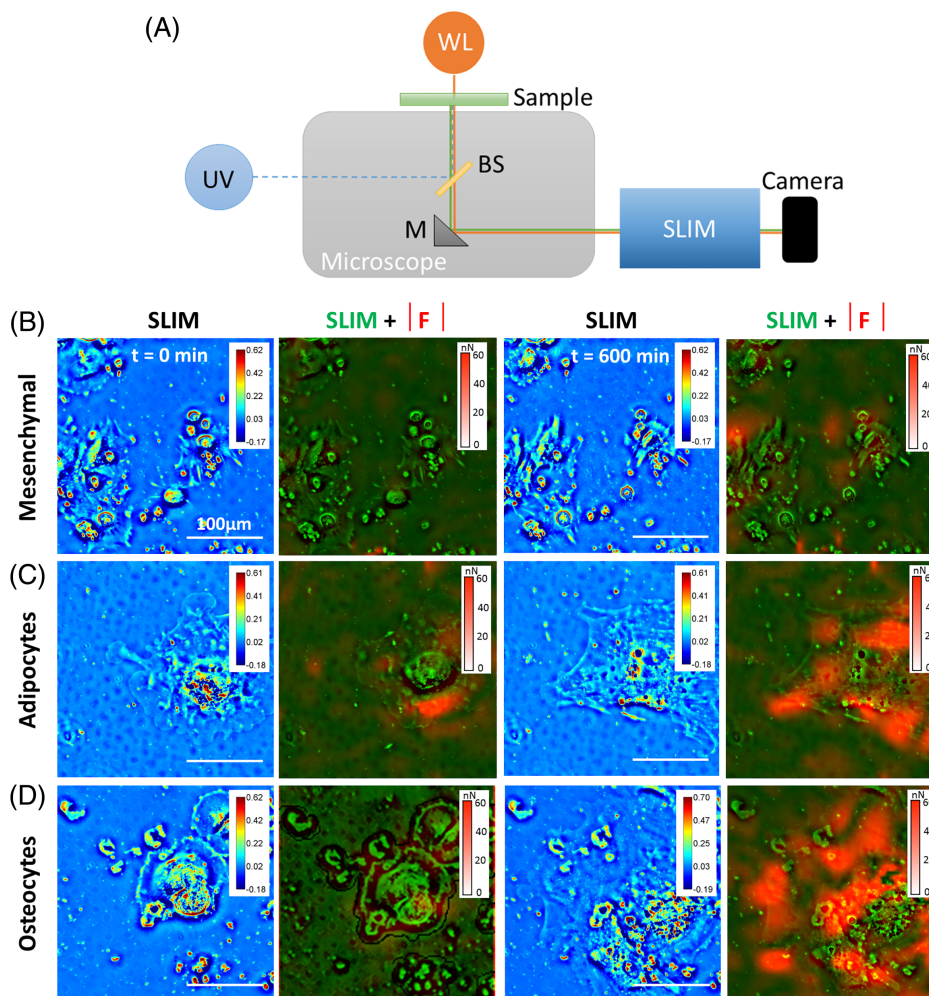


FIGURE 4 Simultaneous measurements of cell growth using SLIM and traction force using HPD. (A) An inverted microscope with a common optical train is used for measurement of SLIM in transmission mode and displacement maps for HPD in the epi-fluorescence mode. (B) MSCs imaged using SLIM and traction force (red overlay) calculated using HPD from the epi-fluorescence image of the same field of view overlaid on the phase image (green) at $t = 0$ minute and $t = 600$ minutes. (C) MSC differentiated into adipocytes imaged using SLIM and traction force (red overlay) calculated using HPD from the epi-fluorescence image of the same field of view overlaid on the phase image (green) at $t = 0$ minute and $t = 600$ minutes. (D) MSC differentiated into osteocytes imaged using SLIM and traction force (red overlay) calculated using HPD from the epi-fluorescence image of the same field of view overlaid on the phase image (green) at $t = 0$ minute and $t = 600$ minutes. $N = 3$, 43 images collected from each distinct sample with SLIM system. This experiment was replicated three times

details on the differentiation process). We chose to study MSCs because these cells are a promising avenue for autologous therapy, and no technique to date has been able to relate cell-matrix traction and growth during lineage specification. Figure 4 demonstrates that displacement and dry mass density maps can be obtained simultaneously and quantitatively by our method.

Previous reports have shown changes in cytoskeleton structure and contractility in MSCs undergoing osteogenesis or adipogenesis [45], which could lead to changes in FAs and traction force [46]. In order to test the sensitivity of our system, we seeded patterned hydrogels with MSCs that were exposed to either basal, osteogenic, or adipogenic media for 1 to 2 weeks. To confirm differentiation of MSCs, cells were stained after 1 week in differentiation media with Oil Red O to confirm adipogenesis and with alkaline phosphatase to confirm osteogenesis. Figure 4 illustrates the concomitant

measurements of traction and SLIM acquired over 10 hours, with a temporal sampling of 15 minutes. There are clear morphological differences between the three cell types. In particular, the MSCs are significantly smaller in size. The overlays between SLIM and the magnitude of the force field show that the forces applied by the MSCs are the smallest. The results also indicate that the forces exerted by the cells become stronger with time.

Histological staining of MSCs exposed to the different media formulations demonstrates the appearance of alkaline phosphatase in the osteogenic conditions and accumulation of lipid droplets in the adipogenic conditions (Figure 5C). Videos S7-S9 illustrate the real time overlay between the cell mass measurements using SLIM and force measurements using HPD in MSCs, adipocytes and osteoblasts. The histogram of all the measured forces (Figure 5A) indicates that the MSCs apply the lowest mean force and also display the

narrowest spread in force magnitude (22.9 ± 17.1 nN). The largest mean tractions are produced by the adipocytes (51.5 ± 39.2 nN) followed by cells undergoing osteogenesis (36.3 ± 30.4 nN). At the same time, the lowest dry mass growth was shown by the MSCs and the highest by the osteoblasts (Figure 5B).

5 | DISCUSSION

Understanding cell mechanotransduction is important for discerning matrix structure-cell function relationships underlying health and disease. Despite the crucial role of mechanochemical signaling in phenomena such as cell migration, proliferation and differentiation, measuring the cell-generated forces at the interface with the extracellular matrix remains challenging. An ideal method would provide continuous, nondestructive images of the force field applied by cells, over broad spatial and temporal scales while also allowing the study of other native cell behavior. Our combined approach of SLIM and HPD enables simultaneous measurement of changes in cell mass and dynamic traction in real time during the initial stages of lineage specification. This advance provides the first technique where dynamic interactions of cells and their matrix can be queried during cell and tissue level processes in situ. Such studies can be conducted over a time period of up to a few days. While some studies have shown that certain cell lines might be vulnerable to blue light exposures over extended time periods, other studies have been able to measure robust cell growth over extended time periods [30, 47, 48]. This might be a confounding factor that could be addressed in future light tolerance studies for specific cell lines and using that information to adjust interval times between measurements. Another imaging technique was recently shown to detect adhesion points between cells and

the substrate [49, 50]. Results from such modalities are complementary to SLIM-HPD approach as they can inform grid periodicity for more accurate traction force measurements specific to the cell type of interest.

Recent studies using beaded PA hydrogels for traction force microscopy have demonstrated that the magnitude of traction forces are higher when the gels are conjugated with fibronectin, as opposed to laminin or collagen [22, 51]. Therefore, we conjugated fibronectin in patterned grids for our combined SLIM-HPD studies on cellular behavior during differentiation processes. Cells exposed to osteogenic supplements, including ascorbic acid, β -glycerophosphate and dexamethasone, exerted higher traction stress over time compared to MSCs cultured under standard growth media. Cells exposed to adipogenic supplements, including indomethacin, insulin, dexamethasone and isobutylmethylxanthine, exerted significantly higher traction stress compared to both MSCs in growth media and those undergoing osteogenesis. Previous work has demonstrated increased traction stress exerted by cells on microposts during the initial stages of adipogenesis and osteogenesis compared to MSCs [46], thus supporting our observations of increased and more dynamic traction forces during cell differentiation. Fu et al observed an initial spike in traction forces followed by a rapid decay to basal levels for cells undergoing adipogenesis (over 7 days; micropost arrays) [46]. However, our study showed that cells undergoing adipogenesis exerted higher average traction compared to cells undergoing osteogenesis and those under basal conditions. We attribute this variance to differences in experimental conditions: we trypsinized MSCs after 1 week in differentiating media, followed by a transfer to patterned substrates for HPD and SLIM measurements under normal media conditions. We performed our analysis in the absence of

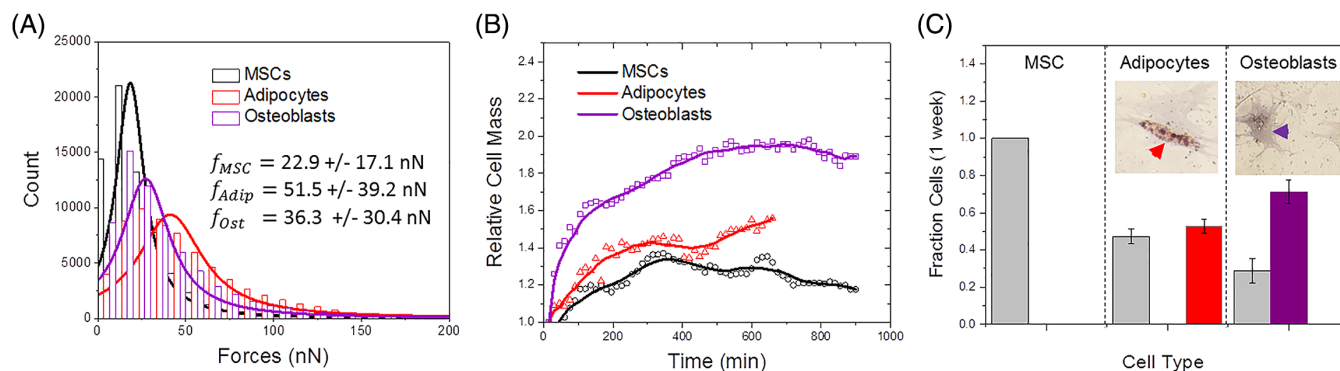


FIGURE 5 Cell lineage specific simultaneous traction force and growth calculations. (A) Histograms showing the distributions of cell traction forces associated with MSC (black), adipocytes (red) and osteoblasts (purple), across the entire experiment. The average magnitude of force exerted by adipocytes was the highest and that of MSCs was the lowest. Differentiated cells demonstrated higher traction force magnitude and dynamic force distribution. $N = 3$, 43 images collected from each distinct sample with SLIM. This experiment was replicated three times. (B) Growth curves displaying the relative cell mass of MSCs, adipocytes and osteoblasts longitudinally through the experiment. Differentiated cells had higher growth rates than MSCs. $N = 3$, 43 images collected from each distinct sample with SLIM. This experiment was replicated three times. (C) At the end of the experiment, cells were stained with Oil Red O+ (red), an adipogenic marker, and ALP+ (purple), a marker for osteogenesis, to verify lineage-specific cell differentiation. $N = 3$, image collected from distinct samples with phase contrast microscope. This experiment was replicated three times. Plots shown represent average of three distinct samples. Error bars indicate SD

hormones to aid the unambiguous assessment of cell-generated force as a function of cell state. We believe that the observed differences in cell traction force are related to the evolution of mechanosensing machinery and the actomyosin network that has previously been shown to accompany specification to adipocyte and osteoblast lineages [52].

Previous studies have demonstrated enhanced proliferation rates in MSCs undergoing differentiation, with the supplements dexamethasone and ascorbic acid playing a clear role in this phenomenon [53, 54]. Multipotent MSCs are known to show a degree of quiescence with low division rates when cultured in niche-mimetic conditions [38, 54, 55]. We observed enhanced cell dry mass growth with adipogenesis > osteogenesis > basal conditions, which is consistent with known relationships between differentiation and proliferation. By simultaneously quantitating traction force using HPD and measuring cell growth with SLIM, we demonstrate the superior reporting capability of this multimodal imaging approach. In our present iteration of this technique, we measure in-plane displacements due to the 2D nature of the fluorescence grid and single focal plane measurements. In principle, this technique can be extended for measurement of out-of-plane displacement by using a three-dimensional fluorescence grid.

This multimodal SLIM-HPD approach enables in situ tracking of relationships between extracellular motif recognition, force transduction and specific bioactivities including growth and differentiation. Thus, we anticipate that our technique will improve understanding of mechanotransduction, especially the interplay between growth and motility.

6 | METHODS

6.1 | Gel preparation

Here, 10 kPa polyacrylamide hydrogels were fabricated by mixing 5% PA (Sigma Aldrich, St. Louis, Missouri) and 0.15% bis-acrylamide (Sigma Aldrich) as previously described [56]. Then, 0.1% ammonium persulfate (Sigma Aldrich, St. Louis, Missouri) and 0.1% tetramethylethylenediamine (Sigma Aldrich, St. Louis, Missouri) were added to the acrylamide mixture and pipetted onto a hydrophobically treated glass slide (Fisher Scientific, Hampshire, UK). An amino-silanized glass cover slip was then flipped onto the solution and allowed to incubate for 20 minutes. Gels were then lifted off and immersed in 55% hydrazine hydrate (Fisher Scientific, Hampshire, UK) for 2 hours to convert amide groups to reactive hydrazide groups, followed by immersion in 5% glacial acetic acid for 1 hour. Gel stiffness was confirmed with AFM as previously described [56]. In order to prepare the substrates for protein patterning and cell adhesion, hydrazine hydrate was used to convert PAAm amide groups to reactive hydrazide groups allowing for the conjugation of ECM proteins via coupling of aldehyde groups formed after oxidation with sodium periodate (Figure 1A).

6.2 | Gel patterning

A patterned master of photoresist (SU-8, Microchem, Westborough, Massachusetts) was created via ultraviolet light through a laser printed mask. PDMS (Polysciences, Inc, Warrington, Pennsylvania) was then polymerized on top of the master to create a stamp with 9 μm spaced grids, such that FITC-conjugated and non-FITC-conjugated adhesion proteins were placed in alternating 9 μm intervals along both the x and y axes. In principle, there is no limitation on grid periodicity provided that it can be resolved by the imaging system. A mixture of 25 $\mu\text{g}/\text{mL}$ of fibronectin and 25 $\mu\text{g}/\text{mL}$ of FITC conjugated fibrinogen was incubated with sodium periodate (Sigma Aldrich, St. Louis, Missouri) for 20 minutes to yield free aldehydes. This incubation took place on top of the patterned PDMS stamp for 30 minutes, air dried and then applied to the surface of the hydrogel, which had been dried in room temperature for 40 minutes (Figure 1B). Next, 25 $\mu\text{g}/\text{mL}$ fibronectin on a blank PDMS stamp was applied onto the hydrogel, following the same procedures as the previous step (Figure 1C). By following these procedures, we obtained a uniform distribution of adhesion proteins on the gel surface for attachment of cell with periodic regions displaying fluorescence signal. The coverslip with the gel was then glued to the bottom of a glass-bottom cell culture dish (MatTek, Ashland, Massachusetts) at two points using tissue adhesion glue (Liquid bandage, CVS).

6.3 | Cell culture and staining

Human MSCs (Lonza, Basel, Switzerland) were allowed to grow until they reached 70% confluency and then seeded onto a six-well plate to initiate differentiation processes. The cells were cultured in MSC growth media (low glucose DMEM, 10% FBS, 5% Pen/Strep, Gibco), adipogenic media (Lonza, Basel, Switzerland) or osteogenic media (Lonza, Basel, Switzerland) for 1 week. Adipogenic media were rotated between induction and maintenance every 3 days. Cells were then lifted off the substrate with 0.25% trypsin (Sigma Aldrich, St. Louis, Missouri) and seeded onto glass-bottom dishes (Figure 1D) and imaged using the multimodal SLIM system. At the end of imaging, to confirm cell lineage, the cells were fixed with 4% paraformaldehyde for 20 minutes and incubated in 60% isopropanol for 5 minutes followed by immersion in Oil Red O working solution (3:2; 300 mg/mL Oil Red O in isopropanol:DI water, Sigma Aldrich) for 10 minutes and then BCIP/NBT (Sigma Aldrich, St. Louis, Missouri) for 10 minutes (Figure 5C).

6.4 | Multimodal SLIM/fluorescence imaging system

SLIM (Cell Vista SLIM Pro; Phi Optics, Inc., Champaign, Illinois) is a QPI system that operates as an add-on module to an existing commercial phase contrast microscope [27, 28, 44]. The back focal plane of the phase contrast objective is projected onto a liquid crystal phase modulator, where programmable phase rings introduce three additional phase shifts, in

increments of $\pi/2$, between the scattered and unscattered light transmitted through the sample. The phase is computed in real time using the corresponding intensity images. Using software developed in-house, the imaging modality can be switched between phase and various fluorescence channels. Thus, we are able to obtain quantitative phase images for cell mass measurements and FITC images for measurement of the deformation fields within the same field of view.

MSCs, adipocytes and osteocytes placed on deformable substrates with fluorescent protein grids were imaged using the phase and FITC module on the SLIM system using a 20X/0.45 numerical aperture (NA) objective. The cells were imaged for 12 hours at 15-minute intervals. Typically, six to eight fields of view were selected from each plate for imaging. The FITC image was taken at the plane of focus for the protein stamp, while the SLIM data were recorded as z-stacks with two frames above and below the plane of focus. This ensures longitudinal integration of dry mass of the cell along its entire thickness. The maximum phase projection through the SLIM z-stack at each time point accounts for changes in cell structure during longitudinal studies. Cell mass was calculated from the phase image using the following relationship, as described in detail in Refs. [30, 48]:

$$\rho(x,y) = \lambda\phi(x,y)/2\pi\gamma, \quad (6)$$

where λ is the central wavelength of the light source, $\phi(x,y)$ is the phase value of the corresponding pixel and $\gamma = 0.2 \text{ mL/g}$ is the refractive index increment of protein [58]. As the mass from multiple cells are averaged for analysis, the mass of each cell at each time point was calculated relative to the first time point (relative cell mass). With this procedure, we eliminate the possibility of a few cells with larger mass dominating the mean mass measurements and therefore, growth trends.

6.5 | Code availability

The code used in this study is available from the corresponding author upon reasonable request.

6.6 | Data availability

The data that support the findings of this study are available from the corresponding author upon reasonable request.

ACKNOWLEDGMENTS

This work was supported by National Science Foundation (NSF) Grants CBET-0939511 STC, DBI 14-50962 EAGER, IIP-1353368 (to G.P.), DMR-1309188 (to A.J.L.), 1454616 CAR (to K.K.) and National Institutes of Health, HL12175 (to K.K.). Y.L. was supported by the National Science Foundation Graduate Research Fellowship Program under Grant No. DGE—1144245.

AUTHOR BIOGRAPHIES

Please see Supporting Information online.

ORCID

Shamira Sridharan Weaver  <https://orcid.org/0000-0003-1997-8941>

Gabriel Popescu  <https://orcid.org/0000-0002-8296-8095>

REFERENCES

- [1] D. H. Boal, *Mechanics of the Cell*, Cambridge University Press, Cambridge, UK, **2002**.
- [2] N. Wang, J. P. Butler, D. E. Ingber, *Science* **1993**, *260*, 1124.
- [3] W. A. Johnson, A. C. B. Harley Eds., *Mechanobiology of Cell-Cell and Cell-Matrix Interactions*, Springer: New York, **2011**.
- [4] K. Wolf, M. te Lindert, M. Krause, S. Alexander, J. te Riet, A. L. Willis, R. M. Hoffman, C. G. Figdor, S. J. Weiss, P. Friedl, *J. Cell Biol.* **2013**, *201*, 1069. <https://doi.org/10.1083/jcb.201210152>.
- [5] K. K. Parker et al., *FASEB J.* **2002**, *16*, 1195.
- [6] S. Stromblad, D. A. Cheresh, *Trends Cell Biol.* **1996**, *6*, 462.
- [7] J. Lee, A. A. Abdeen, K. L. Wycislo, T. M. Fan, K. A. Kilian, *Nat. Mater.* **2016**, *15*, 856. <https://doi.org/10.1038/NMAT4610>.
- [8] J. T. Yang, H. Rayburn, R. O. Hynes, *Development* **1995**, *121*, 549.
- [9] I. Juhasz, G. F. Murphy, H. C. Yan, M. Herlyn, S. M. Albelda, *Am. J. Pathol.* **1993**, *143*, 1458.
- [10] J. E. Frith, R. J. Mills, J. E. Hudson, J. J. Cooper-White, *Stem Cells Dev.* **2012**, *21*, 2442. <https://doi.org/10.1089/scd.2011.0615>.
- [11] V. J. Thannickal, D. Y. Lee, E. S. White, Z. Cui, J. M. Larios, R. Chacon, J. C. Horowitz, R. M. Day, P. E. Thomas, *J. Biol. Chem.* **2003**, *278*, 12384. <https://doi.org/10.1074/jbc.M208544200>.
- [12] W. J. Polacheck, C. S. Chen, *Nat. Methods* **2016**, *13*, 415. <https://doi.org/10.1038/nmeth.3834>.
- [13] J. L. Alonso, W. H. Goldmann, *Life Sci.* **2003**, *72*, 2553. [https://doi.org/10.1016/S0024-3205\(03\)00165-6](https://doi.org/10.1016/S0024-3205(03)00165-6).
- [14] C. Veigel, C. F. Schmidt, *Nat. Rev. Mol. Cell Bio.* **2011**, *12*, 163. <https://doi.org/10.1038/nrm3062>.
- [15] A. R. Bausch, W. Moller, E. Sackmann, *Biophys. J.* **1999**, *76*, 573. [https://doi.org/10.1016/S0006-3495\(99\)77225-5](https://doi.org/10.1016/S0006-3495(99)77225-5).
- [16] R. W. Style, R. Boltyskiy, G. K. German, C. Hyland, C. W. MacMinn, A. F. Mertz, L. A. Wilen, Y. Xu, E. R. Dufresne, *Soft Matter* **2014**, *10*, 4047. <https://doi.org/10.1039/c4sm00264d>.
- [17] I. Schoen, W. Hu, E. Klotzsch, V. Vogel, *Nano Lett.* **2010**, *10*, 1823. <https://doi.org/10.1021/nl100533c>.
- [18] J. L. Tan, J. Tien, D. M. Pirone, D. S. Gray, K. Bhadriraju, C. S. Chen, *Proc. Natl. Acad. Sci. U.S.A.* **2003**, *100*, 1484. <https://doi.org/10.1073/pnas.0235407100>.
- [19] S. Fusco, P. Memmolo, L. Miccio, F. Merola, M. Mugnano, A. Paciello, P. Ferraro, P. A. Netti, *RSC Adv.* **2016**, *6*, 24245. <https://doi.org/10.1039/c5ra26305k>.
- [20] N. Q. Balaban, U. S. Schwarz, D. Riveline, P. Geichberg, G. Tzur, I. Sabanay, D. Mahalu, S. Safran, A. Bershadsky, L. Addadi, B. Geiger, *Nat. Cell Biol.* **2001**, *3*, 466. <https://doi.org/10.1038/35074532>.
- [21] S. R. Polio, K. E. Rothenberg, D. Stamenovic, M. L. Smith, *Acta Biomater.* **2012**, *8*, 82. <https://doi.org/10.1016/j.actbio.2011.08.013>.
- [22] J. Lee, A. A. Abdeen, X. Tang, T. A. Saif, K. A. Kilian, *Biomaterials* **2015**, *69*, 174. <https://doi.org/10.1016/j.biomaterials.2015.08.005>.
- [23] X. Tang, A. Tofangchi, S. V. Anand, T. A. Saif, *PLoS Comput. Biol.* **2014**, *10*, e1003631. <https://doi.org/10.1371/journal.pcbi.1003631>.
- [24] M. Bergert, T. Lendenmann, M. Zündel, A. E. Ehret, D. Panozzo, P. Richner, D. K. Kim, S. J. P. Kress, D. J. Norris, O. Sorkine-Hornung, E. Mazza, D. Poulidakos, A. Ferrari, *Nat. Commun.* **2016**, *7*, 12814. <https://doi.org/10.1038/ncomms12814>.
- [25] H. Colin-York, D. Shrestha, J. H. Felce, D. Waithe, E. Moeendarbary, S. J. Davis, C. Eggeling, M. Fritzsche, *Nano Lett.* **2016**, *16*, 2633. <https://doi.org/10.1021/acs.nanolett.6b00273>.

- [26] S. Makarchuk, N. Beyer, C. Gaiddon, W. Grange, P. Hébraud, *Sci. Rep.* **2018**, *8*, 3038. <https://doi.org/10.1038/s41598-018-21206-2>.
- [27] T. Kim et al., *Nat. Photonics* **2014**, *8*, 256. <https://doi.org/10.1038/Nphoton.2013.350>.
- [28] Z. Wang, L. Millet, M. Mir, H. Ding, S. Unarunotai, J. Rogers, M. U. Gillette, G. Popescu, *Opt. Express* **2011**, *19*, 1016.
- [29] Z. Wang, D. L. Marks, P. S. Carney, L. J. Millet, M. U. Gillette, A. Mihi, P. V. Braun, Z. Shen, S. G. Prasanth, G. Popescu, *Opt. Express* **2011**, *19*, 19907.
- [30] M. Mir, Z. Wang, Z. Shen, M. Bednarz, R. Bashir, I. Golding, S. G. Prasanth, G. Popescu, *Proc. Nat. Acad. Sci. U.S.A.* **2011**, *108*, 13124.
- [31] G. Popescu, *Quantitative Phase Imaging of Cells and Tissues*, McGraw-Hill, New York, **2011**.
- [32] K. J. Chalut, A. E. Ekpenyong, W. L. Clegg, I. C. Melhuish, J. Guck, *Integr. Biol.* **2012**, *4*, 280. <https://doi.org/10.1039/c2ib00129b>.
- [33] J. Guck, S. Schinkinger, B. Lincoln, F. Wottawah, S. Ebert, M. Romeyke, D. Lenz, H. M. Erickson, R. Ananthakrishnan, D. Mitchell, J. Käs, S. Ulvick, C. Bilby, *Biophys. J.* **2005**, *88*, 3689. <https://doi.org/10.1529/biophysj.104.045476>.
- [34] L. Miccio, P. Memmolo, F. Merola, S. Fusco, V. Embrione, A. Paciello, M. Ventre, P. A. Netti, P. Ferraro, *Lab Chip* **2014**, *14*, 1129. <https://doi.org/10.1039/c3lc51104a>.
- [35] A. Tzur, R. Kafri, V. S. LeBleu, G. Lahav, M. W. Kirschner, *Science (New York, N.Y.)* **2009**, *325*, 167. <https://doi.org/10.1126/science.1174294>.
- [36] E. Leith, J. Upatnieks, *JOSA* **1962**, *52*, 1123.
- [37] J. Lee, A. A. Abdeen, K. A. Kilian, *Sci. Rep.* **2014**, *4*, 5188.
- [38] J. Lee, A. A. Abdeen, A. S. Kim, K. A. Kilian, *ACS Biomater. Sci. Eng.* **2015**, *1*, 218. <https://doi.org/10.1021/ab500003s>.
- [39] J. Lee, A. A. Abdeen, D. Zhang, K. A. Kilian, *Biomaterials* **2013**, *34*, 8140. <https://doi.org/10.1016/j.biomaterials.2013.07.074>.
- [40] D. Gabor, *J. Inst. Electr. Eng.* **1946**, *93*, 329.
- [41] D. Gabor, *Nature* **1948**, *161*, 777.
- [42] T. Ikeda, G. Popescu, R. A. Dasari, M. S. Feld, *Opt. Lett.* **2005**, *30*, 1165.
- [43] V. Cerruti, *Ricerche Intorno All'equilibrio de'corpi Elastici Isotropi: Memoria, coi tipi del Salviucci*, Rome, **1882**.
- [44] M. E. Kandel, S. Sridharan, J. Liang, Z. Luo, K. Han, V. Macias, A. Shah, R. Patel, K. Tangella, A. Kajdacsy-Balla, G. Guzman, G. Popescu, *J. Biomed. Opt.* **2017**, *22*, 66016. <https://doi.org/10.1117/1.jbo.22.6.066016>.
- [45] L. MacQueen, Y. Sun, C. A. Simmons, *J. Royal Soc. Interface* **2013**, *10*, 20130179.
- [46] J. Fu, Y. K. Wang, M. T. Yang, R. A. Desai, X. Yu, Z. Liu, C. S. Chen, *Nat. Methods* **2010**, *7*, 733.
- [47] A. Calabuig, M. Mugnano, L. Miccio, S. Grilli, P. Ferraro, *J. Biophotonics* **2017**, *10*, 919. <https://doi.org/10.1002/jbio.201500340>.
- [48] S. Sridharan, M. Mir, G. Popescu, *Biomed. Opt. Express* **2011**, *2*, 2815. <https://doi.org/10.1364/BOE.2.002815>.
- [49] M. Biagio, G. Oriella, M. Valentina, P. Melania, F. Pietro, *J. Biophotonics* **2017**, *10*, 1163. <https://doi.org/10.1002/jbio.201600177>.
- [50] B. Mandracchia, V. Pagliarulo, M. Paturzo, P. Ferraro, *Anal. Chem.* **2015**, *87*, 4124. <https://doi.org/10.1021/acs.analchem.5b00095>.
- [51] J. Lee, A. A. Abdeen, X. Tang, T. A. Saif, K. A. Kilian, *Acta.* **2016**, *42*, 46. <https://doi.org/10.1016/j.actbio.2016.06.037>.
- [52] M. D. Treiser, E. H. Yang, S. Gordonov, D. M. Cohen, I. P. Androulakis, J. Kohn, C. S. Chen, P. V. Moghe, *Proc. Natl. Acad. Sci. U.S.A.* **2010**, *107*(610–615), S610/611. <https://doi.org/10.1073/pnas.0909597107>.
- [53] H. Atmani, D. Chappard, M. F. Basle, *J. Cell. Biochem.* **2003**, *89*, 364. <https://doi.org/10.1002/jcb.10507>.
- [54] K.-M. Choi, Y. K. Seo, H. H. Yoon, K. Y. Song, S. Y. Kwon, H. S. Lee, J. K. Park, *J. Biosci. Bioeng.* **2008**, *105*, 586. <https://doi.org/10.1263/jbb.105.586>.
- [55] D. Zhang, K. A. Kilian, *Biomaterials* **2013**, *34*, 3962. <https://doi.org/10.1016/j.biomaterials.2013.02.029>.
- [56] J. R. Tse, A. J. Engler Preparation of hydrogel substrates with tunable mechanical properties. *Curr Protoc Cell Biol.* **2010** Jun; Chapter 10: Unit 10.16. doi: 10.1002/0471143030.cb1016s47.10.1002/0471143030.cb1016s47.
- [57] J. Lee, A. A. Abdeen, T. H. Huang, K. A. Kilian, *J. Mech. Behav. Biomed. Mater.* **2014**, *38*, 209.
- [58] R. Barer, *Nature* **1953**, *172*, 1097.

SUPPORTING INFORMATION

Additional supporting information may be found online in the Supporting Information section at the end of the article.

Appendix S1 Supplemental Information

Figure S1 Extracting the displacement field of a deformable substrate stamped with a fluorescent 1D grid of 12 micron period. (A) Fluorescent grid showing bending due to cell traction. (B) Zoomed-in region corresponding to the box in A. (C) Fourier transform of the signal in B. (D) Selection of the first Fourier order and centering it at the origin of the spatial frequencies. (E) Phase map associated with displacement of the substrate in the horizontal direction. (F) Displacement field, in microns

Figure S2 (A) True force and displacement maps. (B) Error in the reconstructed force map as a function of force spatial discretization. As expected, the convergence rate is quadratic. (C) Effect of smoothing the displacement maps (low pass filter of wavelength λ , normalized by the cell size h) on the force map error. The error is rather insensitive to smoothing until the low filter pass filter reaches the size of the test cell

Figure S3 Force spatial correlation inside (A) and outside (B) the cells, for mesenchymal cells (left column), osteocytes (middle column) and adipocytes (right column), as indicated. As expected, the spatial correlation is much higher inside the cell than outside, where the calculated forces come from the small noise in the displacement data

Figure S4 Azimuthally averaged profiles through the correlations functions in Figure S1. The 50% decay point of the background (“outside”) correlation function corresponds to a 10 μm , which is close to the 9 μm grid period

Video S1 X and Y displacement maps of a mesenchymal stem cell and the corresponding traction force map

Video S2 X and Y displacement maps of an adipocyte and the corresponding traction force map

Video S3 X and Y displacement maps of an adipocyte and the corresponding traction force map

Video S4 X and Y displacement maps of on osteocyte and the corresponding traction force map

Video S5 X and Y displacement maps of on osteocyte and the corresponding traction force map

Video S6 X and Y displacement maps of on osteocyte and the corresponding traction force map

Video S7 Overlay of traction forces on quantitative phase image of mesenchymal stem cell cluster

Video S8 Overlay of traction forces on quantitative phase image of adipocyte

Video S9 Overlay of traction forces on quantitative phase image of osteocytes

How to cite this article: Sridharan Weaver S, Li Y, Foucard L, et al. Simultaneous cell traction and growth measurements using light. *J. Biophotonics*. 2019;12: e201800182. <https://doi.org/10.1002/jbio.201800182>